Axially Asymmetric Steady State Model of Jupiter's Magnetosphere-Ionosphere Coupling

I. A. Pensionerov[1], S. W. H. Cowley[2], E. S. Belenkaya[1], I. I. Alexeev[1]

[1]Federal State Budget Educational Institution of Higher Education M.V. Lomonosov Moscow State University, Skobeltsyn Institute of Nuclear Physics (SINP MSU), 1(2), Leninskie gory, GSP-1, Moscow 119991, Russian Federation
[2]Department of Physics and Astronomy, University of Leicester, Leicester, UK

Key Points:

- We develop an axially asymmetric model of Jovian magnetosphere-ionosphere coupling
- Comparison of model calculations with observed magnetodisc radial currents suggests an average radial mass transport rate of $\sim$2000 kg s^{-1}
- Inclusion of a nightside partial ring current helps to explain the local time variation of the radial currents

Corresponding author: I. A. Pensionerov, pensionerov@gmail.com

Abstract

We present an axially asymmetric steady state model of Jupiter's magnetosphere-ionosphere coupling with variable ionospheric conductivity dependent on the field-aligned current density. We use Juno and Galileo data to construct a simple model of the equatorial magnetic field, and develop a method for solving the system of partial differential equations describing magnetosphere-ionosphere coupling. Using this model we study the behavior of the system with different radial mass transport rates of magnetospheric plasma and the effect of additional field-aligned currents associated with Jupiter's nightside partial ring current. We compare the model magnetodisc current intensities with those determined directly from magnetic field measurements in various local time sectors, and find that the value of mass transport rate of 2000 kg s^{-1}, larger than usually estimated, better accounts for the observed radial currents. We also find that the inclusion of field-aligned currents associated with Jupiter's partial ring current helps to explain the local time variation of the radial currents, reducing the discrepancy between the model and the observations.

Plain Language Summary

One of the key processes in Jupiter's magnetosphere is the transfer of angular momentum from the planet to the magnetopheric plasma. It is a primary source of energy in the magnetosphere and is thought to be one of the main drivers of the auroral emissions. It was extensively studied using stationary force-balance models. As an approximation, these models assumed axial symmetry, but due to the solar wind influence the structure of Jupiter's magnetosphere is different depending on local time. We present an improved model which partially accounts for this asymmetry. We use it together with Juno and Galileo spacecraft magnetic field measurements to study angular momentum transport at different local times. We found that the observations suggest an approximately twice larger plasma production rate by the moon Io, than is usually estimated. We also show how the asymmetries in the equatorial magnetospheric current can affect the angular momentum transfer.

1 Introduction

Jupiter has a powerful source of plasma deep within the magnetosphere, originating from the volcanic moon Io, which orbits at around 6 R_J. Here R_J = 71,492 km is Jupiter's equatorial 1 bar radius (e.g Joy, 2002). Plasma is transported radially outward from the Io torus, and in the absence of a torque acting on the plasma its angular velocity would fall with radial distance r as $1/r^2$ due to angular momentum conservation. However, the decrease in equatorial plasma angular velocity mapped into the ionosphere increases the collisional friction between ionospheric ions and atmospheric neutrals. In a steady state this torque is balanced by the $\mathbf{j}\times\mathbf{B}$ force of the equatorward ionospheric Pedersen current, with the collisional torque being transferred to the equatorial magnetosphere by field-aligned currents. An equatorial outward radial current acts to enforce corotation via a $\mathbf{j}\times\mathbf{B}$ force and closes the system (Hill, 1979). The effect of the resulting azimuthal field perturbations produced is often described in terms of frozen-in magnetic field lines being "bent back" by the lagging plasma flow. Figure 1 shows the overall current system enforcing corotation. The upward ionospheric field-aligned current region is associated with precipitating electrons and has been suggested to be the source of Jupiter's main oval auroral UV emissions (Cowley & Bunce, 2001; Hill, 2001).

The key parameters of the Hill (1979) model of corotation enforcement are the equatorial magnetic field profile, the plasma mass outflow rate, and the Pedersen conductivity of the ionosphere. The model has been improved and built upon for many years. Pontius (1997) used a realistic magnetic field model that takes into account the current disc field, instead of the simple dipole field used by Hill (1979), to calculate the angular velocity

profile. Hill (2001) and Cowley and Bunce (2001) studied the current system corresponding to the calculated angular velocity profiles and considered its connection to the auroral emissions. Nichols and Cowley (2003) studied the effect of different mass transport rates and ionospheric conductivities on the angular velocity and the currents, while Nichols and Cowley (2004) accounted for ionospheric conductivity modulations by precipitation associated with upward field-aligned current regions. Nichols and Cowley (2005) self-consistently took into account the field-aligned voltages, calculating the plasma angular velocity and currents. They showed that for the Jovian magnetosphere, the difference between the results of the model with and without field-aligned voltages are minor. This problem was later analyzed by Ray et al. (2010), who, on the contrary, found that the influence of field-aligned voltages is not negligible and that they increase the auroral field-aligned currents. Smith and Aylward (2009) developed a self-consistent model of angular momentum transport that includes both magnetosphere and thermosphere. Ray et al. (2015) studied the magnetosphere-ionosphere-thermosphere system and found that the inclusion of field-aligned voltages does not significantly change the dynamics of the thermosphere, while variations in Pedersen conductivity have a strong influence on the system. Cowley et al. (2007) studied the reaction of the Jovian magnetosphere-ionosphere system to a solar wind pressure change and analyzed the variation in power of the accelerated electron precipitation. They found that for major compression the brightness increases, and super-rotation arises, with the M-I coupling current system reversing. Yates et al. (2014) analyzed the influence of solar wind pressure variations on the field-aligned currents, thermospheric flows, heating, and auroral emissions. They concluded that in a steady state the thermosphere becomes hotter as the magnetosphere becomes larger. Tao et al. (2009) investigated the influence of neutral winds on Jovian magnetosphere-ionosphere coupling. They developed an axisymmetric model that includes the thermospheric dynamics, convection, and magnetosphere-ionosphere coupling. Tao et al. (2010) considered the influence of the diurnal variation of the ionospheric conductivity controlled by the solar EUV radiation on the field-aligned currents. According to their results field-aligned currents are strongest at noon, and weakest at dawn. Louarn et al. (2016) studied the empirical relationship between auroral radio emissions and the radial mass transport rate. They found that a larger radial outflow of plasma causes stronger field-aligned currents, and, consequently, more intense auroral activity.

Azimuthal currents in the current disc are determined by radial force balance, and hence depend on the angular velocity profile, while it, in turn, depends on the magnetic field created by the current disc (e.g Arridge & Martin, 2018). Nichols (2011) used the steady state model of radial force balance derived by Caudal (1986) to develop a self-consistent model of the current disc and M-I coupling. Nichols et al. (2015) further developed this model by accounting for anisotropic plasma pressure. They found that the anisotropic pressure component is a dominant or at least not negligible part of the force balance from $\sim$20 R_J to $\sim$50 R_J. Using this model, Nichols et al. (2020) found that an increase in the azimuthal and radial components of the magnetic field and the temperature of the plasma correlates with enhanced brightness of the main auroral oval. They concluded that a transient enhancement can be caused by an increase in the hot magnetospheric plasma pressure and iogenic plasma outflow.

Ray et al. (2014) studied local time (LT) asymmetries of M-I coupling at Jupiter using the Vogt et al. (2011) empirical magnetic field model. While the field model used was LT-dependent, they assumed that M-I coupling is locally axisymmetric. They used an effective ionospheric Pedersen conductivity of 0.1 mho, constant in latitude and LT, and a mass outflow rate of 1000 kg s^{-1}. Lorch et al. (2020) used magnetic field measurements obtained from all the spacecraft that have visited Jupiter to map the average radial and azimuthal current intensities in the magnetodisc in radial distance and LT. Since the radial currents are a key part of the M-I coupling current system, these observations provide an important opportunity to study LT asymmetries at Jupiter.

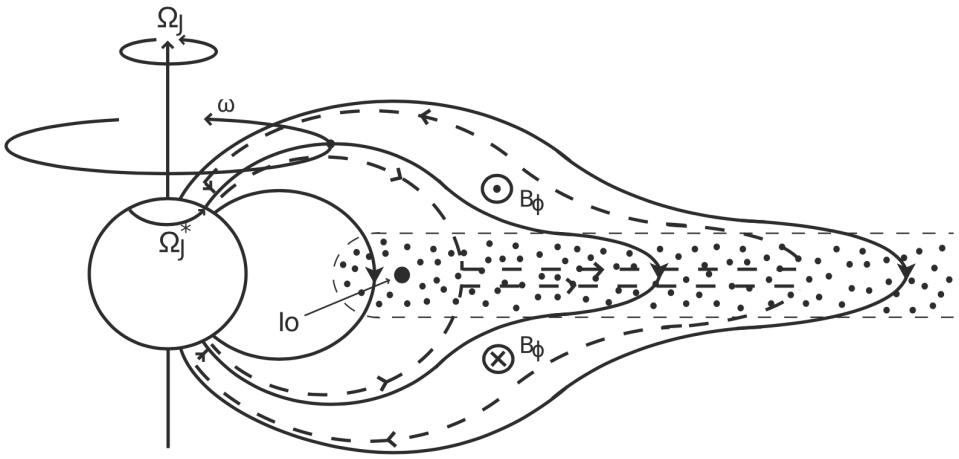

Figure 1. Sketch showing a meridian cross-section through Jupiter's magnetosphere. Arrowed solid lines show magnetic field lines. Arrowed dashed lines show the currents. Ω_J, Ω_J^* and ω are the angular velocities of Jupiter, the upper neutral atmosphere in the ionospheric Pedersen layer, and the plasma in a given flux tube, respectively. The dotted region represents the current sheet plasma. Taken from Nichols (2011), adapted from Cowley and Bunce (2001).

In this paper we develop an axially asymmetric variation of the Hill (1979) model, with variable ionospheric conductivity dependent on the field-aligned current density. In section 2 we derive the model equations. In section 3 we describe the magnetic field model and our approach to solving the differential equations describing M-I coupling. We present the results of the modelling in section 4 and discuss them in section 5. Section 6 summarises our conclusions.

2 Theoretical Background

2.1 Partial Differential Equation for Angular Velocity

In this section we derive the partial differential equation for the plasma angular velocity profile, generalizing previous work to the case of axial asymmetry, thus forming a two dimensional extension of the Hill-Pontius equation (Hill, 1979; Pontius, 1997; Cowley et al., 2002). Calculation of the M-I coupling currents follows Cowley and Bunce (2001), with an angular momentum balance equation derived analogously to that given by Cowley et al. (2002), but now not assuming axial symmetry.

A simple way to map magnetically between the equatorial plane and the ionosphere is provided by Euler's potentials. A magnetic field $\mathbf{B}$ can be expressed in terms of such potentials f and g as

$$\mathbf{B} = \nabla f \times \nabla g. \tag{1}$$

Both f and g are constant along field lines because the magnetic field vector is perpendicular to their gradients. In cylindrical coordinates g is usually chosen in such a way that its isosurfaces are meridians of constant magnetic longitude. We assume $g = \phi$ and $f = F(\rho, \phi, z)$. The model field is hence wholly poloidal with zero azimuthal component. Function F is magnetic flux per unit azimuthal angle and is sometimes called the flux function. With this assumption

$$B_z = \frac{1}{\rho}\frac{\partial F}{\partial \rho}. \tag{2}$$

For purposes of modeling we consider the internal magnetic field of the planet to be dipolar, for which function F_d is given by

$$F_d = B_J \rho^2 \left(\frac{R_J}{r} \right)^3, \tag{3}$$

where ρ is the cylindrical distance from the magnetic axis, r is the distance from the center of the planet, and B_J is Jupiter's equatorial magnetic field strength ($B_J = 4.17 \times 10^5$ nT in the JRM09 internal field model of Connerney et al. (2018)). Near the planetary surface the internal planetary field is dominant, so that assuming the planet is approximately spherical, the ionospheric F_i is

$$F_i = \rho_i^2 B_J, \tag{4}$$

where ρ_i is the perpendicular distance from the magnetic axis in the ionospheric layer. Since f is constant along a field line, we can map between the magnetospheric equator and the ionosphere using

$$F_e(\rho, \phi) = F_i(\rho_i, \phi). \tag{5}$$

From current continuity, the structure of the current system shown in Figure 1, and the assumption of north-south symmetry it follows that on a given flux shell in a given azimuthal sector

$$\rho i_\rho = 2 \rho_i i_P, \tag{6}$$

where i_ρ is the radial current intensity in the equatorial current disc integrated through its north-south width, and i_P is the ionospheric height-integrated Pedersen current intensity given by

$$i_P = 2 B_J \rho_i \Sigma_P^* (\Omega_J - \omega). \tag{7}$$

Here we have assumed that the polar planetary field is near-vertical and of strength $2B_J$ (instead of the strict dipole formula $B_r = 2B_J \cos\theta$). $\Omega_J = 1.76 \times 10^{-4}$ rad s^{-1} is Jupiter's angular velocity, ω is the ionospheric plasma angular velocity, and Σ_P^* is the effective height-integrated ionospheric Pedersen conductivity. The effective conductivity accounts for rotational lagging of the neutral atmosphere relative to rigid corotation due to ion-neutral collisions, and is reduced compared to the true value by an unknown factor $0 < (1-k) < 1$, taken to be equal 0.5 following Achilleos et al. (1998) and previous related works (e.g., Cowley & Bunce, 2001; Cowley et al., 2002; Nichols & Cowley, 2004). From equations (4)–(7) we obtain

$$\rho i_\rho = 4 \Sigma_P^* F_e (\Omega_J - \omega). \tag{8}$$

We assume that the equatorial plasma is concentrated in a thin disc. The angular momentum per unit mass of the equatorial plasma is $\rho^2 \omega(\rho, \phi)$, where ω is angular velocity. The flux of angular momentum is caused by radial transport of the plasma and its rotation around the planet. The change of angular momentum per unit time in the volume between ρ and $\rho + d\rho$ and inside the sector centered at azimuthal angle ϕ with angular width $d\phi$ is

$$dT_z = \frac{\partial(\dot{M}_\rho \rho^2 \omega)}{\partial \rho} \frac{d\phi}{2\pi} + \frac{\partial(\dot{M}_\phi \rho^2 \omega)}{\partial \phi} d\rho, \tag{9}$$

where $\dot{M}_\rho$ is the radial mass transport rate per 2π radians of azimuth (full equatorial circle), and $\dot{M}_\phi$ is the azimuthal mass transport rate per unit radial length. The Lorentz force torque per unit volume about Jupiter's center is $\mathbf{r} \times (\mathbf{j} \times \mathbf{B})$, where $\mathbf{r}$ is the position vector, $\mathbf{j}$ is the current density, and $\mathbf{B}$ is the magnetic field. If B_ρ varies only slowly with ρ on the scale of the sheet thickness, and B_ϕ varies only slowly with ϕ, then div$\mathbf{B} = 0$ guarantees that B_z varies only slowly with z on the scale of the sheet thickness. Then the z-component of the torque acting on the plasma inside the volume element considered is

$$dT_z = -\rho^2 i_\rho B_z d\rho d\phi. \tag{10}$$

If the mass density of the plasma per unit area of the equatorial current sheet is $D(\rho, \phi)$ then

$$\dot{M}_\phi = \rho\omega D. \tag{11}$$

Substitution of equations (10) and (11) into the equation (9) gives

$$\frac{\partial(\dot{M}_\rho \rho^2 \omega)}{\partial \rho}\frac{1}{2\pi} + \rho^3 \frac{\partial(\omega^2 D)}{\partial \phi} = -\rho^2 i_\rho B_z. \tag{12}$$

We then substitute the width-integrated radial current given by equation (8) into equation (12) to obtain the following partial differential equation for the angular velocity

$$\frac{\partial(\dot{M}_\rho \rho^2 \omega)}{\partial \rho}\frac{1}{2\pi} + \rho^3 \frac{\partial(\omega^2 D)}{\partial \phi} = -4\Sigma_P^* \rho B_z F_e(\Omega_J - \omega). \tag{13}$$

Throughout the paper we will assume $\dot{M}_\rho$ to be constant at all local times (we discuss this assumption in section 5), which means that $\frac{\partial(\dot{M}_\rho)}{\partial \rho} = 0$. With this assumption from continuity of the mass flow

$$\mathrm{div}(D\mathbf{v}) = 0\,, \tag{14}$$

where $\mathbf{v}$ is plasma bulk velocity, we find

$$\frac{\partial(\omega D)}{\partial \phi} = 0\,. \tag{15}$$

We then can simplify equation (13) to get

$$\frac{\dot{M}_\rho}{2\pi}\frac{\partial(\rho^2\omega)}{\partial \rho} + D\rho^3\omega\frac{\partial \omega}{\partial \phi} = -4\Sigma_P^* \rho B_z F_e(\Omega_J - \omega). \tag{16}$$

Physically correct solutions must converge to almost rigid corotation close to the planet, thus the boundary condition is

$$\omega(\rho_{\mathrm{inner}}, \phi) \approx \Omega_J, \tag{17}$$

where ρ_{inner} is any ρ inside the region of nearly rigid corotation. In this paper ρ_{inner} is taken to be $6\,R_J$ (near the orbit of Io).

2.2 Modulation of Ionospheric Conductivity by Field-Aligned Currents

The ionospheric Pedersen conductivity is modulated by precipitation of electrons accelerated by field-aligned voltages in the auroral region. Nichols and Cowley (2004), using the results of Millward (2002), calculated how the height-integrated ionospheric Pedersen conductivity depends on the outward field-aligned currents density, and provided the following analytic approximation

$$\Sigma_P(j_{||i}) = 0.16 j_{||i} + 2.45 \times \left(\frac{(j_{||i}/0.075)^2}{1 + (j_{||i}/0.075)^2}\right) \times \frac{1}{1 + \exp\left(-\frac{(j_{||i} - 0.22)}{0.12}\right)}\,, \tag{18}$$

where $j_{||i}$ is the field-aligned current density just above the ionospheric layer. The effective conductivity is then

$$\Sigma_P^* = (1 - k)(\Sigma_P(j_{||i}) + \Sigma_{P0}), \tag{19}$$

where Σ_{P0} is the background height-integrated ionospheric Pedersen conductivity taken to be 0.1 mho (Nichols & Cowley, 2004).

If we assume the absence of electric currents perpendicular to the magnetic field lines in the region between the current disc and the ionosphere, then $j_{||}/B$ is constant

along the field lines. Following Cowley et al. (2002) we then find the equatorial field-aligned current density from the divergence of the radial currents

$$\frac{j_{||}}{B} = \frac{j_z}{B_e} = -\frac{1}{2B_z}\frac{1}{\rho}\frac{d}{d\rho}\left(4\Sigma_P^* F_e(\Omega_J - \omega)\right). \tag{20}$$

If there exists a partial ring current in Jupiter's magnetosphere, we should add the divergence of the azimuthal magnetodisc currents $\nabla_\phi i_\phi$ to the equation to obtain

$$\frac{j_{||}}{B} = \frac{j_z}{B_e} = -\frac{1}{2B_z}\left(\frac{1}{\rho}\frac{d}{d\rho}\left(4\Sigma_P^* F_e(\Omega_J - \omega)\right) + \nabla_\phi i_\phi\right). \tag{21}$$

We will later define these additional field-aligned currents explicitly as an input parameter for the model. The ionospheric field-aligned current density is then

$$j_{||i} = -\frac{B_J}{B_z}\left(\frac{1}{\rho}\frac{d}{d\rho}\left(4\Sigma_P^* F_e(\Omega_J - \omega)\right) + \nabla_\phi i_\phi\right). \tag{22}$$

Equations (16) and (22) constitute a system of partial differential equations (PDEs) for ω and $j_{||i}$. Their solution requires a second boundary condition at some distance ρ_{j0}

$$j_{||i}(\rho_{j0}, \phi) = j_{||i0}(\phi). \tag{23}$$

Ideally we would like to set $\rho_{j0} = \rho_{\text{inner}}$ and solve system of equations (16) and (22) radially outward from ρ_{inner}. But this system is unstable in the near-rigid corotation region and is nearly impossible to solve this way. In the next section we will discuss the reasons for this in detail and describe our approach to obtaining approximate solutions.

3 Modeling Approach

3.1 Magnetic Field Model

The model equatorial magnetospheric magnetic field employed has been derived from Galileo and Juno magnetometer data, using data from all Galileo orbits and from Juno perijoves 0–22 that are currently available. As in Lorch et al. (2020), we split the data into eight 3 h wide LT sectors, yielding sufficient data to cover radial distances of interest, and allowing us to readily compare our results with those of Lorch et al. (2020). For our purposes we are interested only in the equatorial magnetic field. To determine whether or not a data point is inside the current disc we used two conditions. The first one requires spacecraft to be closer than 4 R_J to the center of the sheet according to the Khurana and Schwarzl (2005) model. We use a large half-width of 4 R_J instead of the commonly used value of 2–2.5 R_J because sheet crossings predicted by Khurana and Schwarzl (2005) are often shifted from the observed ones. The second condition requires the ρ-component of the magnetic field to be smaller than 2 nT. Its purpose is to select the real crossings from the broad intervals picked by the first condition. In each LT sector we fitted the polynomial

$$B_n(\rho) = \frac{a}{\rho} + \frac{b}{\rho^2} + \frac{c}{\rho^3} \tag{24}$$

to the component of the residual magnetic field, that is normal to the local current sheet surface. The residual field was obtained by subtracting the JRM09 model of the internal planetary field (Connerney et al., 2018) from the data. (We note that for the modelling we still used a dipolar internal magnetic field because of the assumed north-south symmetry and the neglect of dipole tilt). Because local time sector 9 h is not covered by Juno and Galileo trajectories beyond 40 R_J we were unable to get a valid fit for it. We instead used an average of two neighboring sectors (6 h and 12 h) fits. Figure 2 shows the data and the fit for the midnight sector.

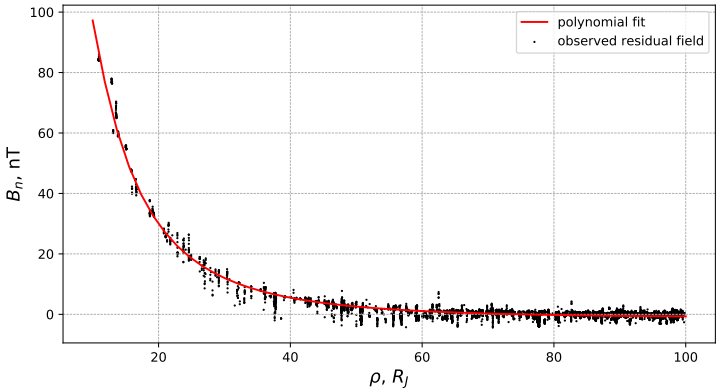

Figure 2. Black dots show the component of the residual magnetic field normal to the current sheet for the 3 h LT sector centered on 00/24 h. The residual magnetic field is obtained by subtracting the internal field according to the JRM09 model of the internal planetary field (Connerney et al., 2018) from the data. The red line shows the polynomial fit given by equation (24) with coefficients listed in Table 1.

Table 1. Coefficients of the polynomial given by equation (24), fitted to the residual z component of the equatorial magnetic field in LT sectors 00 to 21 h. Coefficients used by Lorch et al. (2020) are shown for comparison.

LT	a, $10^2 \cdot$ nT	b, $10^4 \cdot$ nT	c, $10^4 \cdot$ nT
00	-2.859	2.280	-10.217
03	-2.944	2.351	-10.529
06	-1.983	1.923	-8.492
09	-2.504	1.941	-8.540
12	-3.025	1.958	-8.588
15	-4.653	2.327	-10.894
18	-5.876	2.783	-13.039
21	-4.450	2.352	-9.776
Lorch et al.	-1.825	1.893	-8.441

Because of the sparsity of data in the inner region and to avoid divergence for $\rho < 10\ R_J$ we used the current disc field model developed by Pensionerov et al. (2019) instead of the polynomial given by equation (24), smoothing the transition between the two field regimes by linear interpolation. Table 1 lists the coefficients of the polynomial used in the LT sectors 00 to 21 (labeled by their central local time value), while Figure 3 shows the resulting approximation combined with the dipolar magnetic field and its magnetic colatitude mapping. Function F for this field model was then obtained by integrating equation (2) from the small non-zero value of $\rho = 0.01\,R_J$ to the local ρ value. Because we use the magnetic field model as an input for the system of equations (16) and (22), we solve it on a fine ρ grid, but in 3 h wide LT sectors. The outer boundary for our solutions is set to be at $70\,R_J$.

3.2 Method for Obtaining Numerical Solutions

Most of the Hill-Pontius differential equation solutions quickly diverge to very large positive or negative values of angular velocity in the inner magnetosphere. The phys-

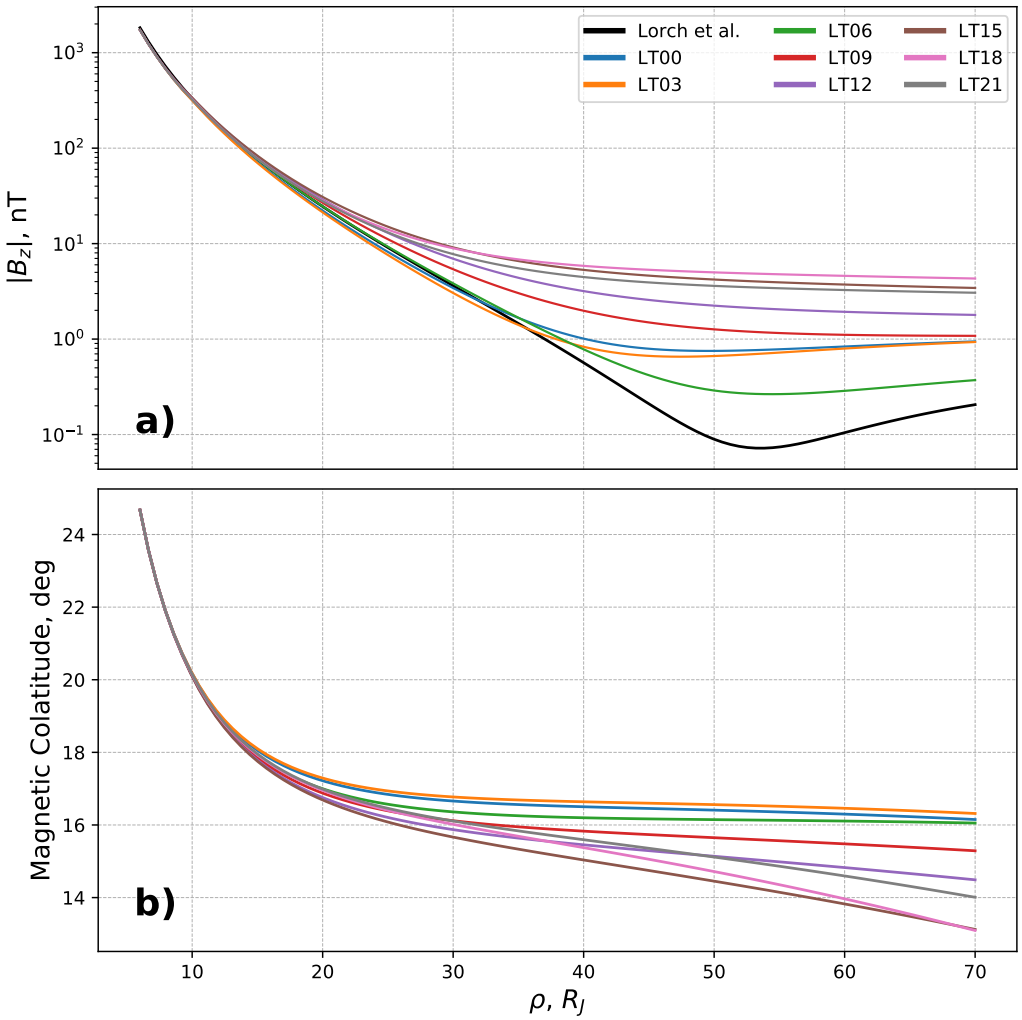

Figure 3. Panel (a) shows the absolute value of the z component of the equatorial magnetic field obtained by combining the dipolar field and the polynomial approximation of the residual magnetic field given by equation (24) with the coefficients used in the present model for LT sectors 00 to 21 h (Table 1). We also show the field profile derived by Lorch et al. (2020). Within 10 R_J the Pensionerov et al. (2019) current disc field model is used. Panel (b) shows the magnetic mapping of ionospheric colatitude as a function of equatorial radial distance for the model shown.

ically correct solution converges to $\sim \Omega_J$. In the one-dimensional case with an explicitly defined ionospheric conductivity function $\Sigma_P^*(\rho)$, the solution can easily be obtained by solving the equation radially outward with the boundary condition $\omega(\rho_{\text{inner}}) = \Omega_J$. This is because solutions with slightly different boundary conditions near the planet quickly converge to the one solution we are interested in as shown in the appendix of Cowley and Bunce (2003).

This approach cannot be applied to the Hill-Pontius equation combined with the equation for ionospheric conductivity modulation by field-aligned currents, because it becomes unstable in the inner region. Since we cannot start the solution from the rigid corotation region, we cannot ensure the fulfillment of $\omega(\rho_{\text{inner}}) = \Omega_J$ by solving the equations radially outward. Nichols and Cowley (2004) deal with this problem by solving the equations radially inward. A solution obtained in this way eventually diverges to large negative or positive angular velocity, with the physically correct solution sitting in-between. This family of solutions maps to a range of boundary conditions, where larger boundary angular velocities correspond to the solutions diverging upward and the smaller ones to the solutions diverging downward. It allows to use binary search to find the boundary value that corresponds to rigid corotation near the planet. Nichols and Cowley (2004) fixed the field-aligned current at a distance of $100\,R_J$ and binary searched the physically correct angular velocity. Tracing the solution deep inside the near-rigid corotaion region requires the boundary value to be specified to a large number of digits, quickly exceeding the 64-bit float accuracy. Nichols and Cowley (2004) traced the solution to 10–20 R_J and used an approximate iterative solution in the inner region. The same can be done with a fixed angular velocity and binary-searched field-aligned current boundary condition.

The method for solving the one dimensional Hill-Pontius equation with an explicit conductivity can easily be adapted to the two dimensional case. However, the Nichols and Cowley (2004) method for the equation with variable conductivity cannot, because the binary search becomes impossible due to the influence of the azimuthal sectors on each other. The crux of the issue lies in the second term of equation (16) that accounts for the net azimuthal transport of angular momentum $D\rho^3\omega\frac{\partial\omega}{\partial\phi}$. It is useful, therefore, to estimate the significance of this term in comparison with the other terms. For this purpose, as well as later for obtaining the solutions, we need an estimate of the plasma mass density. We employed the profile of cold plasma concentration per unit magnetic flux from Nichols (2011), which together with our magnetic field model yields the number density per unit area, and hence the mass density per unit area assuming an average ion mass of 20 amu.

To estimate the significance of azimuthal transport we used the Hill (1979) analytical angular velocity profile applicable in case of a purely dipolar magnetic field, because it is generally representative of the plasma angular velocity behavior at Jupiter. We also assumed an upper bound for the azimuthal derivative of ω to be $0.5\times(\Omega_J - \omega)$, consequent on the fact that as the angular velocity converges towards rigid corotation, its azimuthal derivative should converge towards zero. The choice of the coefficient 0.5 is based on estimates of the derivative obtained by solving the one-dimensional system of equations for each LT separately. Using these assumptions, we compared the electromagnetic torque (the right hand side of equation (16)) with the azimuthal transport term. Figure 4 shows a comparison using Hill's solution with a characteristic distance $\rho_H = 25\,R_J$ (the distance at which the angular velocity starts to deviate significantly from rigid corotation). The azimuthal transport term becomes less significant the closer we get to the planet. This means that in the region with ρ less than some boundary ρ_B we can neglect the second term in equation (16) and solve the system of equations (16) and (22) for each LT sector using the Nichols and Cowley (2004) method. Ideally we would like ρ_B to be as small as possible to better justify the neglect of the azimuthal transport term. But we need ρ_B to be large enough for the boundary conditions search to be pos-

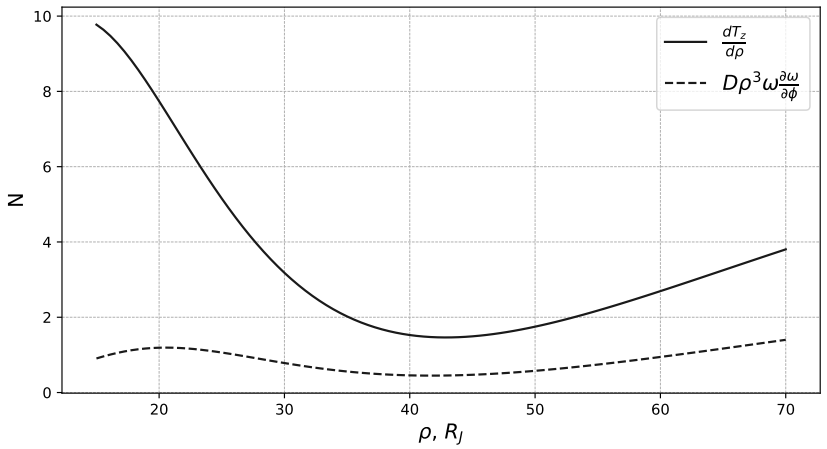

Figure 4. Comparison of terms in equation (16), where the solid line shows the electromagnetic torque term while the dashed line shows an estimate of the net azimuthal transport of angular momentum term.

sible. We picked $\rho_B = 25\,R_J$ as it was the smallest that worked reliably for the search. The result varies with the plasma density and ρ_H, but in most cases the azimuthal angular momentum transport effect is at least several times less than the electromagnetic torque effect in the region $\rho < 25\,R_J$.

From ρ_B the solutions are traced inwards to 15 R_J. Tracing to the region closer to the planet becomes too computationally intensive. To obtain the solution in the region from 6 to 15 R_J we interpolate the field-aligned currents at the 15 R_J boundary to zero at 10 R_J using a cubic spline. We then calculate the corresponding ionospheric conductivity and use it explicitly to solve the simple Hill-Pontius equation radially outward in the 6 to 15 R_J region. Because the field-aligned currents at 15 R_J are comparatively small, the combined solution is practically continuous.

Finally, we use the values of ω and $j_{||i}$ at ρ_B which for each LT sector correspond to a solution that converges to approximately Ω_J in the inner region as boundary conditions to solve the system of equations (16) and (22) at $\rho > \rho_B$. We solve it radially outward on a fine ρ grid in the same 3 h wide LT sectors. We no longer neglect the net azimuthal transport term, using the full left hand side of equation (16). This approach usually yields a valid solution, though, depending on the magnetic field profile and the chosen fixed boundary condition, it can produce angular velocities and field-aligned currents diverging to large positive values.

3.3 Boundary Conditions

As mentioned above, the Nichols and Cowley (2004) method for selecting boundary conditions requires one of them to be fixed. The specific value for it is dictated by the observations. At the moment we do not have detailed time-averaged measurements of the angular velocity at $\rho_B = 25\,R_J$. Recently, Lorch et al. (2020) derived the divergence of the observed magnetodisc currents, which we could use for our boundary conditions. However it is calculated as a finite difference of the observed currents, and while the statistical errors of the currents themselves are relatively small, for the divergence they become significant. Instead of the divergence, we opted to use Lorch et al. (2020) radial current measurments directly. Using equations (8) and (19) we can constrain the

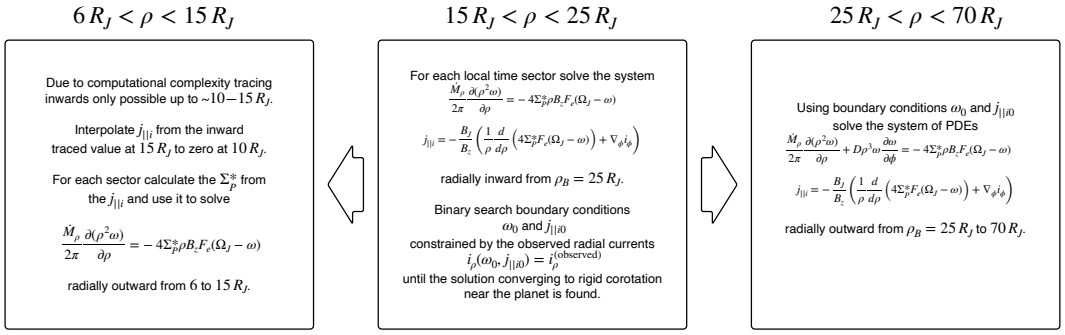

Figure 5. Diagram outlining the algorithm for obtaining solutions to the system of equations (16) and (22).

boundary conditions by the observed radial current

$$i_\rho(\omega_0, j_{||i0}) = i_\rho^{(\mathrm{observed})}. \tag{25}$$

The binary search works slightly differently than in the case when one of the values is fixed. We conducted the search for $j_{||i}$, while the corresponding ω was calculated from equation (25) on each iteration. Not every value of the radial current has a solution converging to near-rigid corotation. We found that one of the important factors determining whether or not such a solution exists for a given boundary radial current is the value of $\dot{M}_\rho$. For example, with $\dot{M}_\rho = 1000$ kg s^{-1} the observed radial currents are typically too large and the equation has no physically correct solutions. In such cases we iteratively decreased the boundary radial currents from the observed value, each time conducting a new search, until a valid solution became possible. Figure 5 shows a diagram, outlining the algorithm for for obtaining the solutions.

4 Results

4.1 Solutions Without Field-Aligned Currents from the Partial Ring Current

We now examine the solutions obtained using the method described in section 3, and compare the model magnetodisc radial current intensities with those determined by Lorch et al. (2020). The key model parameter is the radial mass transport rate $\dot{M}_\rho$. For simplicity we assume it to be symmetrical in LT and constant with ρ (we discuss these assumptions in section 5). Here we compare solutions for the canonical $\dot{M}_\rho$ value of 1000 kg s^{-1}, and an increased value of 2000 kg s^{-1}.

In Figure 6 we compare the width-integrated radial current intensities calculated from the model results for $\dot{M}_\rho = 1000$ kg s^{-1} (blue lines) and 2000 kg s^{-1} (orange) with the observed current intensities from Lorch et al. (2020) (black) in the LT sectors from 00 to 21 h. For each sector the root-mean-square deviation (RMSD) of the model currents from the observed ones is given. The major observation here is that the 1000 kg s^{-1} model systematically underestimates the observed currents within ~40 R_J in all local times except noon. The 2000 kg s^{-1} model, on the other hand, comes closer to the observed values in this region, especially in sectors 00/24, 03, 15 and 21 h. However it still underestimates the currents in the 06, 09 and 18 h sectors. The noon sector likely has a radial mass transport rate lower than 1000 kg s^{-1}, as both models overestimate the currents there.

In the region closer than $\sim 15\,R_J$ in some sectors the observed radial currents become negative, most prominently at 21, 00/24, and 03 h. Radial currents in our model

always converge to zero near the planet and so it cannot explain these observations. Beyond 40 R_J, the behavior of the observed currents changes depending on LT. In the midnight-dawn sector the radial current intensities tend to decrease with radial distance very slowly, while in the dusk sector and at 09 h they decrease significantly faster. The model currents are generally more similar in behavior to the observed currents in the dawn sector than in the dusk sector. In the LT sectors 00–09 h the 2000 kg s^{-1} model has 40-50% smaller RMSD than the 1000 kg s^{-1} model. In sectors 12–21 h the situation is opposite, though less pronounced: the 1000 kg s^{-1} model has 10-25% smaller RMSD than the 2000 kg s^{-1} model.

Figure 7 demonstrates the angular velocities, ionospheric field-aligned currents, and effective conductivity for the 2000 kg s^{-1} and 1000 kg s^{-1} cases. Model field-aligned currents in LT sectors 15, 18 and 21 h rapidly increase beyond $\sim 50 R_J$, while the angular velocity falls very slowly or even trends back towards rigid corotation. This is not supported by observations and is likely an artefact of the model, caused by the assumption of constant radial mass outflow and the absence of additional field-aligned currents. These features disappear when we incorporate field-aligned currents from the partial ring current into the calculations in the next section. At some local times there is a noticeable derivative discontinuity at ρ_B in all of the variables. This is the result of neglecting azimuthal transport for $\rho < \rho_B$. These discontinuities are not severe, which indicates that our approximation was justified.

Angular velocities in the case of 2000 kg s^{-1} start to deviate significantly from rigid corotation slightly closer to the planet than for the case of 1000 kg s^{-1}, thus producing stronger radial currents. The ionospheric field-aligned currents and conductivity behave similarly for both radial mass transport values. Field-aligned currents are typically in the range 0.1–0.2 μA m^{-2}, with peaks in the dawn sector at 20–30 R_J reaching 0.4–0.5 μA m^{-2}. The corresponding effective conductivities range from 0.1 to 1.3 mho.

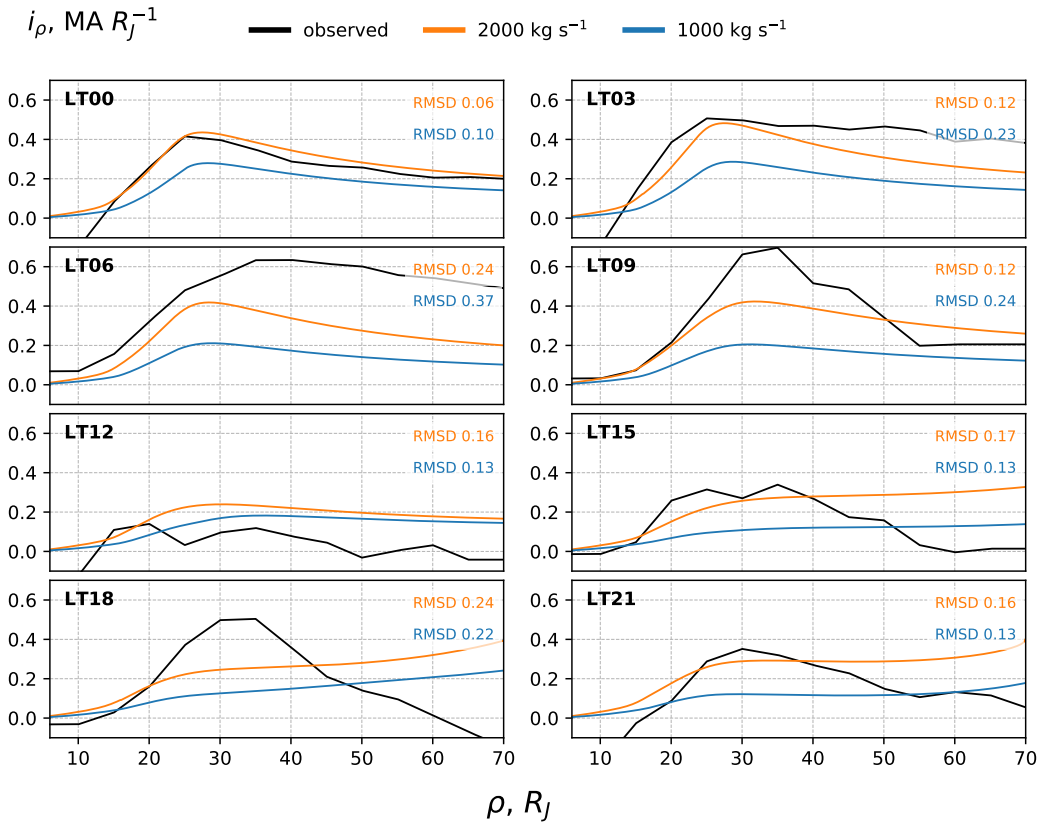

Figure 6. Equatorial width-integrated radial current intensities plotted versus distance ρ from the planetary magnetic axis in 3 h wide LT sectors centered on 00–21 h. Black lines show the empirical currents derived from magnetic field data by Lorch et al. (2020), while the blue and orange lines show model currents for $\dot{M}_\rho$=1000 and 2000 kg s^{-1}, respectively. The root-mean-square deviation (RMSD) of the model current from the observed current is shown for both model values.

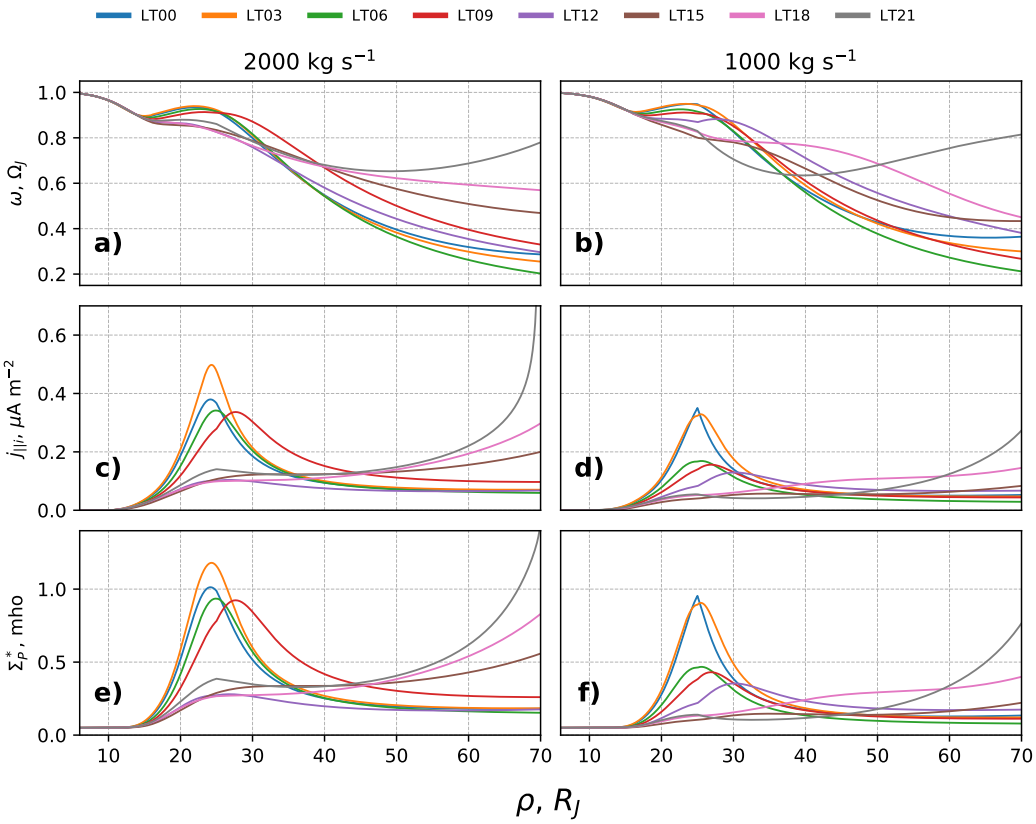

Figure 7. Panels (a) and (b) show angular velocities, (c) and (d) ionospheric field-aligned current densities, and (e) and (f) effective height-integrated ionospheric conductivities, for each LT sector. Panels on the left correspond to a mass transport rate of 2000 kg s^{-1}, while the panels on the right correspond to 1000 kg s^{-1}. All parameters are plotted versus equatorial distance from the planetary rotation axis, mapped along field lines in the case of the ionospheric parameters in panels (c)–(f).

Table 2. Parameters A and ρ_c of the approximate form for the ionospheric field-aligned currents associated with the partial ring current given by equation (26), as employed in LT sectors 00 to 21 h for the models with radial mass outflow rates of 2000 kg s^{-1} and 1000 kg s^{-1}

LT	2000 kg s^{-1}		1000 kg s^{-1}	
	A, μA m^{-2}	ρ_c, R_J	A, μA m^{-2}	ρ_c, R_J
00	0.00	30	0.00	30
03	-0.10	30	-0.10	30
06	-0.20	30	-0.10	30
09	0.00	30	0.00	30
12	0.00	30	0.00	30
15	0.08	30	0.05	35
18	0.10	31	0.05	35
21	0.10	30	0.05	35

4.2 Solutions with Field-Aligned Currents from the Partial Ring Current

While Lorch et al. (2020) provide the divergence of the observed azimuthal equatorial current, this divergence, as discussed above, comes with significant statistical errors. The solutions of the Hill-Pontius equation with variable conductivity are very sensitive not only to the magnitude of the ionospheric field-aligned currents, associated with the divergence of the azimuthal currents ($(\nabla_\phi i_\phi)_i$ for brevity), but also to their radial derivatives. The variation of the observed divergence from one bin to the next caused by the said errors, usually renders the equations unsolvable. Thus, instead of using the observed divergences to calculate $(\nabla_\phi i_\phi)_i$ directly, we employed a simple parametric equation.

We found that the radial currents tend to increase when the radial derivative of $(\nabla_\phi i_\phi)_i$ is positive and to decrease when its negative. This is, to a certain degree, expected, because the ionospheric conductivity increases with the density of the field-aligned currents, and the radial currents are proportional to the conductivity. According to Lorch et al. (2020), the azimuthal current is removed from the magnetodisc in the dawn sector and added back to it in the dusk sector. Removal and addition correspond to negative and positive $(\nabla_\phi i_\phi)_i$, respectively. If we now assume that $(\nabla_\phi i_\phi)_i$ decreases in magnitude with distance from the planet, the sign of its derivative becomes consistent with the observed behavior of the radial currents at dawn and dusk. In the dusk sector the derivative of $(\nabla_\phi i_\phi)_i$ becomes negative, which can explain the faster decrease of the observed radial currents there. The opposite is true at dawn, where the positive derivative slows the decrease of radial currents with distance. On these grounds, we use the following equation for $(\nabla_\phi i_\phi)_i$

$$(\nabla_\phi i_\phi)_i = A\rho_c \frac{\tanh\left(\frac{\rho-\rho_c+d}{d}\right)+1}{\rho+\rho_c}\,. \tag{26}$$

Parameter d was set to be $5\,R_J$, while the chosen values of ρ_c and A for each LT are presented in Table 2. This equation smoothly interpolates to zero at distances smaller than ρ_c, with the smoothness of interpolation controlled by d (as we assume the azimuthal currents become symmetrical in the inner magnetosphere) and its absolute value falls as $1/\rho$ at greater distances. The specific values of ρ_c and A were chosen to best fit the observed radial currents with the model ones. The form of the approximation as well as its parameters are somewhat arbitrary, so we only aim to qualitatively study the effects

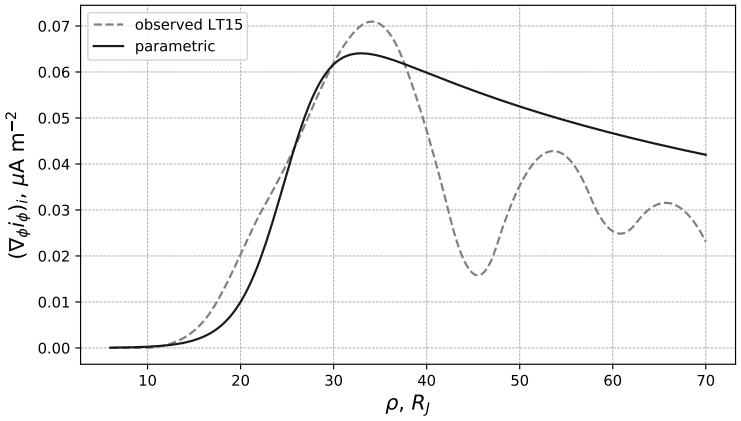

Figure 8. Field-aligned current from the partial ring current versus distance from the magnetic axis for 15 h LT. The solid line shows the parametric approximation given by equation (26) with $A = 0.08$ μA m^{-2} and $\rho_c = 30$ R_J, corresponding to the 2000 kg s^{-1} case in Table 2, while the dashed line shows the field-aligned current calculated from the observed currents from Lorch et al. (2020). Inside 20 R_J the observed azimuthal current divergence was not taken into account due to relatively large errors, and was linearly interpolated to zero from the boundary value. Beyond 20 R_J the observed divergence was interpolated by quadratic splines.

of $(\nabla_\phi i_\phi)_i$. Figure 8 shows an example of $(\nabla_\phi i_\phi)_i$ at 15 h LT calculated using equation (26) (solid line), together with $(\nabla_\phi i_\phi)_i$ calculated from observations (dashed line).

Figure 9 shows the radial currents in the same format as Figure 6, but with $(\nabla_\phi i_\phi)_i$ included. In sectors 12 and 00/24 h LT the addition of $(\nabla_\phi i_\phi)_i$ did not improve the fit, so we didn't include $(\nabla_\phi i_\phi)_i$ in the final calculations. For the midnight and noon sectors such an assumption seems plausible, because for a nightside partial ring current we expect $(\nabla_\phi i_\phi)_i$ to be present mostly at dawn and dusk. $(\nabla_\phi i_\phi)_i$ also didn't improve the fit at 09 h LT. In this sector the observed $(\nabla_\phi i_\phi)_i$ is strongly negative, so if its magnitude decreases with distance its derivative is positive. As stated above, this leads to the model radial current falling slower than for the case without $(\nabla_\phi i_\phi)_i$, while the observed current at 09 h, on the contrary, decreases very sharply. This behavior might be a result of a change in the radial mass transport rate with distance, unaccounted for in the present model. It also should be noted that, as indicated above, the 09 h sector has substantially less spacecraft coverage, which means that our magnetic field model and the Lorch et al. (2020) results might be inaccurate. Because of this we set $(\nabla_\phi i_\phi)_i$ to zero in this sector as well.

In the rest of the sectors $(\nabla_\phi i_\phi)_i$ significantly decreases the RMSD of the model with both radial mass transport values. For $\dot{M}_\rho = 2000$ kg s^{-1} RMSD is 40–60% lower. For $\dot{M}_\rho = 1000$ kg s^{-1} the change is less dramatic with RMSD 10–40% lower than in the case without $(\nabla_\phi i_\phi)_i$. Although the addition of $(\nabla_\phi i_\phi)_i$ generally increases the model radial currents in the 1000 kg s^{-1} case, this value still significantly underestimates the observations within $\sim$40 R_J. For 2000 kg s^{-1} the improvement in RMSD mostly comes from the region outside 40 R_J. With $\dot{M}_\rho = 2000$ kg s^{-1} our model describes the Lorch et al. (2020) results very well in sectors 00/24, 03, 06 and 21 h. While the fit in sectors 15 and 18 h was significantly improved (reducing the RMSD twofold), the model still does not fit the observations beyond 40 R_J well. Overall, the 2000 kg s^{-1} model has significantly lower RMSD than the 1000 kg s^{-1} model at most local times.

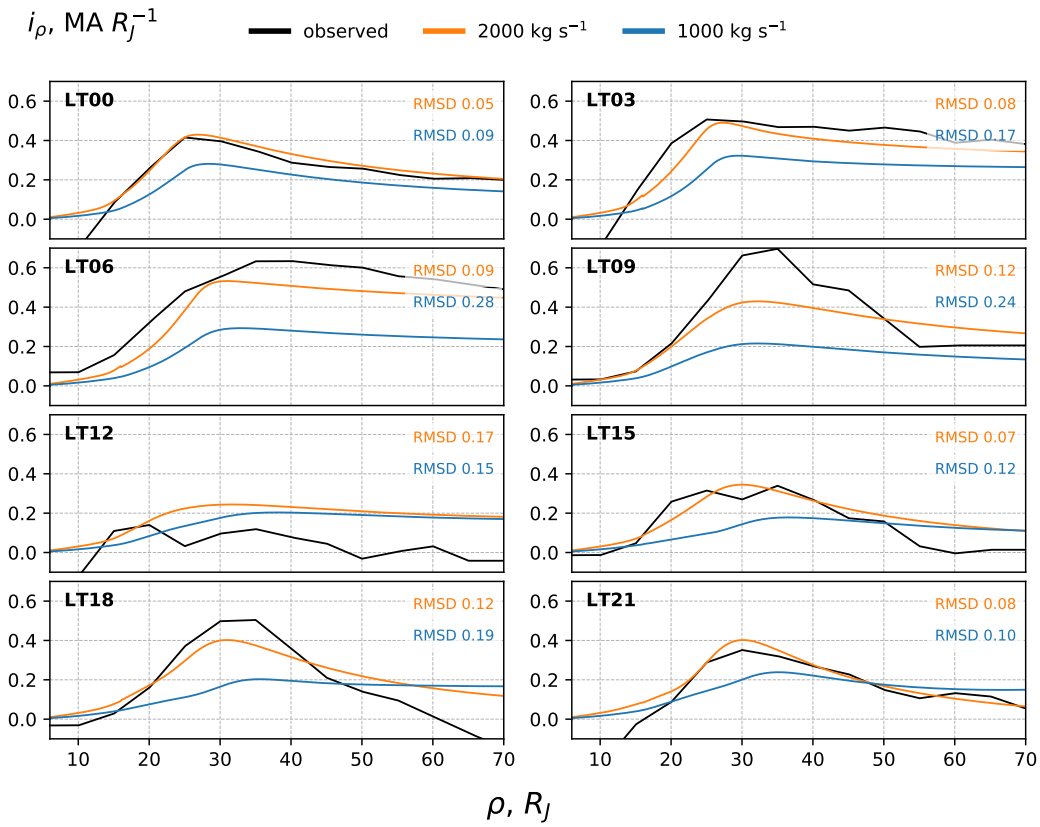

Figure 9. Same as Figure 6, but for the models including field-aligned currents from the partial ring current.

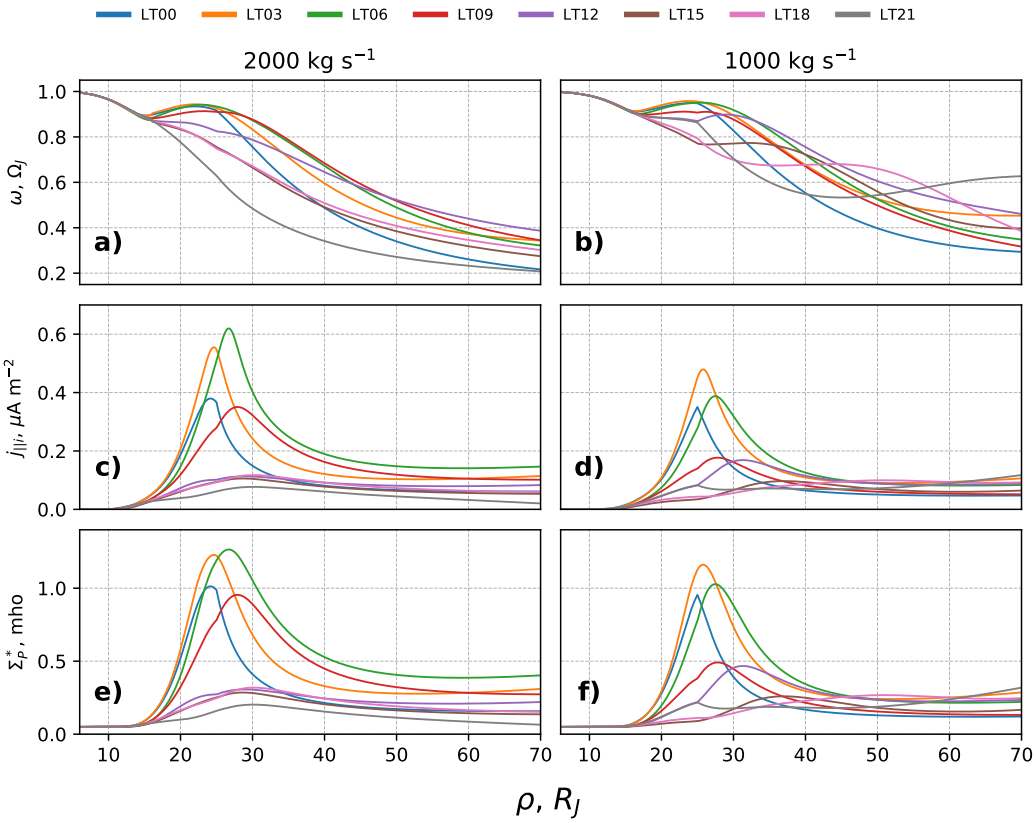

Figure 10. Same as Figure 7, but for the models including field-aligned currents from the partial ring current.

Figure 10 demonstrates the angular velocities, ionospheric field-aligned currents, and effective conductivity in the same format as Figure 7, but for the model including $(\nabla_\phi i_\phi)_i$. The anomalies in the dusk sector with diverging angular velocities are no longer present. Although the results changed for the individual sectors, the ranges and the behavior of all variables remain generally the same, with the dawn sector still having larger field-aligned currents peaks at 20–30 R_J than the dusk sector.

5 Discussion

A key feature of steady state M-I coupling models is their relative simplicity, compared to full 2D or 3D MHD modelling. This simplicity allows one to test the response of the system to different values of various parameters with low iteration time and computing power requirements, and to compare the results with observations. Here we have developed a variation of this model which is asymmetrical in LT. This allows us to compare the radial equatorial current intensities calculated using the model with those determined from magnetic field measurements by Lorch et al. (2020) in eight 3 h wide LT sectors centered on 00 to 21 h.

In this work we compared the equatorial radial currents produced by the model using radial mass outflow rates of 1000 and 2000 kg s^{-1}, and found that the model currents are in significantly better agreement with observations when a transport rate of 2000 kg s^{-1} is used. Currents produced in the 1000 kg s^{-1} case are systematically lower than those observed. This result is unexpected, with most estimates of radial mass outflow rate being lower. In Jupiter's magnetosphere the transport rate is generally assumed to be equal to the Io plasma production rate. Various empirical estimates of the plasma production rate have been made, ranging from 150 to 2000 kg s^{-1} (Broadfoot et al., 1981; Vasyliunas, 1983; Bagenal, 1997; Bagenal & Delamere, 2011), and the canonical value of 1000 kg s^{-1} has been used in many previous related works (Cowley & Bunce, 2001; Cowley et al., 2002; Nichols, 2011; Ray et al., 2014; Nichols et al., 2015). Nichols et al. (2020) used the canonical value as representative of the typical outflow rate, while using 2350 kg s^{-1} for an enhanced plasma production case. Hill (2001) used the value of 2000 kg s^{-1} in his calculations, while Nichols and Cowley (2003) studied solutions of the Hill-Pontius equation for various outflow rates from 100 to 10000 kg s^{-1}.

The magnetic field observations used by Lorch et al. (2020) to calculate the currents, and those employed by us to construct our model of the magnetospheric equatorial field, are taken from observations made on the trajectories of several spacecraft, thus representing a time-averaged picture. We then take the mass transport rates used in our modelling to correspond to the average mass transport rate in the system and hence cannot explain the 2000 kg s^{-1} value as temporarily enhanced.

Another potential explanation comes from our neglect of the changes of mass outflow rate with distance from the planet. This can change the results in many different ways, as both the radial derivative of the outflow and the extra azimuthal flow created are a part of the differential equations. Our model fits the data better in the nightside magnetosphere, where the approximation of constant outflow is probably closer to reality. The inclusion of a variable outflow rate is one of the prime avenues for further research. However, the model with the canonical outflow rate of 1000 kg s^{-1} underestimates the observations even within 20 R_J, where the variability of radial outflow is probably much less pronounced, than in the outer regions. Thus we find the outflow variability with distance unlikely to remove the discrepancy.

We also neglected B_ϕ in our calculations. It does not directly affect the angular momentum balance, but can "bend" the azimuthal sectors, changing the effective magnetic field profile. Because the model with 1000 kg s^{-1} underestimates the observed cur-

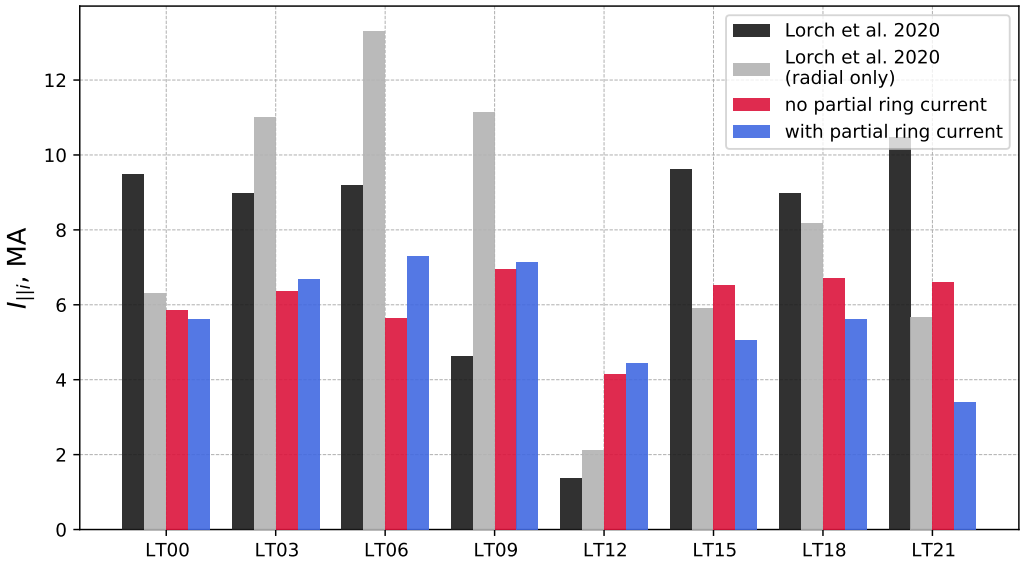

Figure 11. Upward field-aligned currents integrated over the ionosphere in one hemisphere for each 3 h wide LT sector. Black and gray bars show the Lorch et al. (2020) observations with and without azimuthal currents divergence, while the red and blue bars show results without and with field-aligned currents from the partial ring current, respectively. A 2000 kg s^{-1} mass outflow rate is used for the model results.

rents across almost all of the local times, we find this change unlikely to affect our conclusions and leave it for future work.

Nichols and Cowley (2004) compared their calculated radial currents with those derived from Galileo azimuthal magnetic field data obtained in the midnight LT sector, and found that the model currents better fit the observed values with $\dot{M}_\rho$ set to a larger value of 2000 or 3000 kg s^{-1}. We used the same approximation for the conductivity dependence on the field-aligned ionospheric current density as Nichols and Cowley (2004), as well as the same atmosphere slippage coefficient of 0.5, which affects the effective conductivity. Preliminary tests with a lower slippage coefficient and hence higher effective conductivity did not show an increase in the model radial currents, while tests with a higher coefficient and consequent lower effective conductivity showed a decrease in currents. From this it follows that changes in the slippage coefficient do not alter the systematic underestimation of the observed currents by the 1000 kg s^{-1} model. However, more rigorous study is needed on the behavior of the solutions with different approximations for the conductivity dependence on the field-aligned current.

We also considered the effect of field-aligned currents from the partial ring current on the solutions. Because they are sensitive to the radial derivatives of $(\nabla_\phi i_\phi)_i$, we were unable to use the observed divergences directly. Instead we used a simple analytic form for the resulting ionospheric field-aligned currents with parameters individually selected for each LT sector. The direction of the field-aligned currents we used is in agreement with the Lorch et al. (2020) observations. The inclusion of these currents in the model allowed us to significantly improve the agreement between the observed and model equatorial radial currents, reducing the root-mean-square deviation by 40–60% in most local times. However, both the form of the approximation and the specific parameters are to an extent arbitrary, with only the sign of the currents being directly tied to the observations. So while the inclusion of such currents *can* help to explain the variation of

radial currents behavior between dawn and dusk sector, it not necessarily *does*. At local times 09, 15 and 18 h the inclusion of extra field-aligned currents was not sufficient to explain the sharp decrease in observed radial currents. As stated above, a possible way to improve the model in this regard would be to account for mass transport rate variations with the distance from the planet.

Bonfond et al. (2015) used HST images to estimate the brightness asymmetry of the main oval of Jupiter's UV aurora. They found that in the southern hemisphere the dusk sector emission is on average ~ 3 times brighter than in the dawn sector, while in the northern hemisphere the dusk sector is only ~ 1.1 times brighter (possibly due to the northern magnetic anomaly complicating the analysis). As a possible explanation of this asymmetry, Bonfond et al. (2015) suggested the presence of a partial ring current in the nightside magnetosphere, whose field-aligned currents would strengthen the main oval aurora at dusk while weakening it at dawn. The calculations by Ray et al. (2014) are inconsistent with the Bonfond et al. (2015) results, since they predict stronger field-aligned currents in the dawn sector. Our calculations also show stronger field-aligned currents in the dawn sector. However, the total upward field-aligned current is not larger in the dawn sector, because in the dusk sector it covers a significantly wider latitude range. Figure 11 shows the upward field-aligned current integrated over the ionosphere in one hemisphere for each of the 3 h wide LT sectors. This figure shows our results for cases with and without $(\nabla_\phi i_\phi)_i$ as well as the Lorch et al. (2020) observations with and without azimuthal current divergence. We integrated over the ionospheric colatitudes that correspond to the equatorial radial distances range $6\,R_J < \rho < 55\,R_J$, to avoid the diverging model currents in the case without $(\nabla_\phi i_\phi)_i$. The model current is 20–50% smaller than the observed current at all local times other than noon. For the model currents in both cases and for the full observed current there is no strong dawn-dusk asymmetry. From these results it follows that the additional field-aligned currents from the partial ring current do not necessarily affect the aurora in the simple way suggested by Bonfond et al. (2015). Additional field-aligned currents change the conductivity of the ionosphere, which in turn changes the angular velocity profile, and hence the field-aligned currents from the divergence of the radial currents. In the LT sectors 15, 18 and 21 h, which have positive $(\nabla_\phi i_\phi)_i$, the total positive field-aligned current is less than in the case without $(\nabla_\phi i_\phi)_i$, while in the 03 and 06 h LT sectors, which have negative $(\nabla_\phi i_\phi)_i$, the total is larger. The resulting field-aligned currents depend strongly on the magnitude and radial derivative of the additional currents.

6 Conclusions

We have presented an axially asymmetrical variant of the steady state M-I coupling model for the Jovian magnetosphere. We have compared the radial magnetodisc currents calculated using this model with those derived by Lorch et al. (2020) from in situ magnetic field observations.

1. We found that the observed radial current magnitudes require an average radial mass transport rate of 2000 kg s^{-1}, significantly higher than the value typically used of 1000 kg s^{-1}.
2. We considered the effect of field-aligned currents associated with the nightside partial ring current on the M-I coupling system. We found that their inclusion allows a partial explanation of the diurnal variations of the magnetodisc radial currents, reducing the discrepancy between the model and observations by 10–60%, depending on the local time.

A notable simplification in the present model is the assumption of a constant radial mass transport rate with the distance from the planet. Accounting for changes in the mass transport rate with distance is one of the directions for future work.

Acknowledgments

Work at the Lomonosov Moscow State University was supported by Ministry of Science and Higher Education of the Russian Federation under the grant 075-15-2020-780 (N13.1902.21.0039). Work at the University of Leicester was supported by UKRI/STFC Consolidated Grant ST/N000749/1.

Magnetometer data used in this study was retrieved from the Planetary Data System database (`https://pds-ppi.igpp.ucla.edu/`) using

1. Files `fgm\_jno\_l3\_YYYYDDDpc\_r60s\_v01` from the `JNO-J-3-FGM-CAL-V1.0` dataset (`https://doi.org/10.17189/1519711`)
2. Files `ORBXX_SYS3.TAB` from the `GO-J-MAG-3-RDR-MAGSPHERIC-SURVEY-V1.0` dataset (`https://doi.org/10.17189/1519668`).

Ancillary calculations were made with the SPICE Toolkit via SpiceyPy (`https://doi.org/10.21105/joss.02050`).

References

Achilleos, N., Miller, S., Tennyson, J., Aylward, A. D., Mueller-Wodarg, I., & Rees, D. (1998). JIM: A time-dependent, three-dimensional model of jupiter's thermosphere and ionosphere. *Journal of Geophysical Research: Planets*, *103*(E9), 20089–20112. Retrieved from `https://doi.org/10.1029/98je00947`

Arridge, C. S., & Martin, C. J. (2018). Current sheets at the giant planets. In *Electric currents in geospace and beyond* (pp. 191–205). John Wiley & Sons, Inc. Retrieved from `https://doi.org/10.1002/9781119324522.ch12`

Bagenal, F. (1997). The ionization source near io from galileo wake data. *Geophysical Research Letters*, *24*(17), 2111–2114. Retrieved from `https://doi.org/10.1029/97gl02052`

Bagenal, F., & Delamere, P. A. (2011). Flow of mass and energy in the magnetospheres of jupiter and saturn. *Journal of Geophysical Research: Space Physics*, *116*(A5). Retrieved from `https://doi.org/10.1029/2010ja016294`

Bonfond, B., Gustin, J., Gérard, J.-C., Grodent, D., Radioti, A., Palmaerts, B., ... Tao, C. (2015, October). The far-ultraviolet main auroral emission at jupiter - part 1: Dawn-dusk brightness asymmetries. *Annales Geophysicae*, *33*(10), 1203–1209. Retrieved from `https://doi.org/10.5194/angeo-33-1203-2015`

Broadfoot, A. L., Sandel, B. R., Shemansky, D. E., McConnell, J. C., Smith, G. R., Holberg, J. B., ... Bertaux, J. L. (1981). Overview of the voyager ultraviolet spectrometry results through jupiter encounter. *Journal of Geophysical Research: Space Physics*, *86*(A10), 8259–8284. Retrieved from `https://doi.org/10.1029/ja086ia10p08259`

Caudal, G. (1986). A self-consistent model of Jupiter's magnetodisc including the effects of centrifugal force and pressure. *Journal of Geophysical Research*, *91*(A4), 4201.

Connerney, J. E. P., Kotsiaros, S., Oliversen, R. J., Espley, J. R., Joergensen, J. L., Joergensen, P. S., ... Levin, S. M. (2018). A new model of Jupiter's magnetic field from Juno's first nine orbits. *Geophysical Research Letters*, *45*(6), 2590–2596. Retrieved from `https://doi.org/10.1002/2018gl077312`

Cowley, S. W. H., & Bunce, E. (2001). Origin of the main auroral oval in jupiter's coupled magnetosphere-ionosphere system. *Planetary and Space Science*, *49*(10-11), 1067–1088. Retrieved from `https://doi.org/10.1016/s0032-0633(00)00167-7`

Cowley, S. W. H., & Bunce, E. J. (2003, January). Modulation of jovian middle magnetosphere currents and auroral precipitation by solar wind-induced compressions and expansions of the magnetosphere: initial response and

steady state. *Planetary and Space Science*, *51*(1), 31–56. Retrieved from https://doi.org/10.1016/s0032-0633(02)00130-7

Cowley, S. W. H., Nichols, J. D., & Andrews, D. J. (2007, June). Modulation of jupiter's plasma flow, polar currents, and auroral precipitation by solar wind-induced compressions and expansions of the magnetosphere: a simple theoretical model. *Annales Geophysicae*, *25*(6), 1433–1463. Retrieved from https://doi.org/10.5194/angeo-25-1433-2007

Cowley, S. W. H., Nichols, J. D., & Bunce, E. J. (2002). Distributions of current and auroral precipitation in jupiter's middle magnetosphere computed from steady-state hill–pontius angular velocity profiles: solutions for current sheet and dipole magnetic field models. *Planetary and Space Science*, *50*(7-8), 717–734. Retrieved from https://doi.org/10.1016/s0032-0633(02)00046-6

Hill, T. W. (1979). Inertial limit on corotation. *Journal of Geophysical Research*, *84*(A11), 6554. doi: 10.1029/ja084ia11p06554

Hill, T. W. (2001). The jovian auroral oval. *Journal of Geophysical Research: Space Physics*, *106*(A5), 8101–8107. Retrieved from https://doi.org/10.1029/2000ja000302

Joy, S. P. (2002). Probabilistic models of the Jovian magnetopause and bow shock locations. *Journal of Geophysical Research*, *107*(A10). Retrieved from https://doi.org/10.1029/2001ja009146

Khurana, K. K., & Schwarzl, H. K. (2005). Global structure of jupiter's magnetospheric current sheet. *Journal of Geophysical Research: Space Physics*, *110*(A7). Retrieved from https://agupubs.onlinelibrary.wiley.com/doi/abs/10.1029/2004JA010757

Lorch, C. T. S., Ray, L. C., Arridge, C. S., Khurana, K. K., Martin, C. J., & Bader, A. (2020). Local time asymmetries in jupiter's magnetodisc currents. *Journal of Geophysical Research: Space Physics*, *125*(2). Retrieved from https://doi.org/10.1029/2019ja027455

Louarn, P., Kivelson, M. G., & Kurth, W. S. (2016, October). On the links between the radio flux and magnetodisk distortions at jupiter. *Journal of Geophysical Research: Space Physics*, *121*(10), 9651–9670. Retrieved from https://doi.org/10.1002/2016ja023106

Millward, G. (2002). On the dynamics of the jovian ionosphere and thermosphere III. the modelling of auroral conductivity. *Icarus*, *160*(1), 95–107. Retrieved from https://doi.org/10.1006/icar.2002.6951

Nichols, J. D. (2011). Magnetosphere-ionosphere coupling in Jupiter's middle magnetosphere: Computations including a self-consistent current sheet magnetic field model. *Journal of Geophysical Research: Space Physics*, *116*(A10).

Nichols, J. D., Achilleos, N., & Cowley, S. W. H. (2015). A model of force balance in Jupiter's magnetodisc including hot plasma pressure anisotropy. *Journal of Geophysical Research: Space Physics*, *120*(12), 10,185-10,206. Retrieved from https://doi.org/10.1002/2015ja021807

Nichols, J. D., Allegrini, F., Bagenal, F., Bunce, E. J., Cowley, S. W. H., Ebert, R. W., ... Yao, Z. (2020, August). An enhancement of jupiter's main auroral emission and magnetospheric currents. *Journal of Geophysical Research: Space Physics*, *125*(8). Retrieved from https://doi.org/10.1029/2020ja027904

Nichols, J. D., & Cowley, S. W. H. (2003). Magnetosphere-ionosphere coupling currents in jupiter's middle magnetosphere: dependence on the effective ionospheric pedersen conductivity and iogenic plasma mass outflow rate. *Annales Geophysicae*, *21*(7), 1419–1441. Retrieved from https://doi.org/10.5194/angeo-21-1419-2003

Nichols, J. D., & Cowley, S. W. H. (2004). Magnetosphere-ionosphere coupling currents in jupiter's middle magnetosphere: effect of precipitation-induced enhancement of the ionospheric pedersen conductivity. *Annales Geophysicae*, *22*(5), 1799–1827. Retrieved from https://doi.org/10.5194/

711 angeo-22-1799-2004
712 Nichols, J. D., & Cowley, S. W. H. (2005, March). Magnetosphere-ionosphere cou-
713 pling currents in jupiter's middle magnetosphere: effect of magnetosphere-
714 ionosphere decoupling by field-aligned auroral voltages. *Annales Geo-*
715 *physicae*, *23*(3), 799–808. Retrieved from https://doi.org/10.5194/
716 angeo-23-799-2005
717 Pensionerov, I. A., Alexeev, I. I., Belenkaya, E. S., Connerney, J. E. P., & Cowley,
718 S. W. H. (2019). Model of jupiter's current sheet with a piecewise current
719 density. *Journal of Geophysical Research: Space Physics*, *124*(3), 1843–1854.
720 Retrieved from https://doi.org/10.1029/2018ja026321
721 Pontius, D. H. (1997). Radial mass transport and rotational dynamics. *Journal*
722 *of Geophysical Research: Space Physics*, *102*(A4), 7137–7150. Retrieved from
723 https://doi.org/10.1029/97ja00289
724 Ray, L. C., Achilleos, N. A., Vogt, M. F., & Yates, J. N. (2014, June). Local time
725 variations in jupiter's magnetosphere-ionosphere coupling system. *Journal*
726 *of Geophysical Research: Space Physics*, *119*(6), 4740–4751. Retrieved from
727 https://doi.org/10.1002/2014ja019941
728 Ray, L. C., Achilleos, N. A., & Yates, J. N. (2015, August). The effect of includ-
729 ing field-aligned potentials in the coupling between jupiter's thermosphere,
730 ionosphere, and magnetosphere. *Journal of Geophysical Research: Space*
731 *Physics*, *120*(8), 6987–7005. Retrieved from https://doi.org/10.1002/
732 2015ja021319
733 Ray, L. C., Ergun, R. E., Delamere, P. A., & Bagenal, F. (2010, September).
734 Magnetosphere-ionosphere coupling at jupiter: Effect of field-aligned poten-
735 tials on angular momentum transport. *Journal of Geophysical Research: Space*
736 *Physics*, *115*(A9), n/a–n/a. Retrieved from https://doi.org/10.1029/
737 2010ja015423
738 Smith, C. G. A., & Aylward, A. D. (2009). Coupled rotational dynamics of jupiter's
739 thermosphere and magnetosphere. *Annales Geophysicae*, *27*(1), 199–230. Re-
740 trieved from https://doi.org/10.5194/angeo-27-199-2009
741 Tao, C., Fujiwara, H., & Kasaba, Y. (2009, August). Neutral wind control of the
742 jovian magnetosphere-ionosphere current system. *Journal of Geophysical Re-*
743 *search: Space Physics*, *114*(A8), n/a–n/a. Retrieved from https://doi.org/
744 10.1029/2008ja013966
745 Tao, C., Fujiwara, H., & Kasaba, Y. (2010, February). Jovian magneto-
746 sphere–ionosphere current system characterized by diurnal variation of iono-
747 spheric conductance. *Planetary and Space Science*, *58*(3), 351–364. Retrieved
748 from https://doi.org/10.1016/j.pss.2009.10.005
749 Vasyliunas, V. M. (1983). Plasma distribution and flow. In *Physics of the jovian*
750 *magnetosphere* (pp. 395–453). Cambridge University Press. Retrieved from
751 https://doi.org/10.1017/cbo9780511564574.013
752 Vogt, M. F., Kivelson, M. G., Khurana, K. K., Walker, R. J., Bonfond, B., Gro-
753 dent, D., & Radioti, A. (2011, March). Improved mapping of jupiter's auroral
754 features to magnetospheric sources. *Journal of Geophysical Research: Space*
755 *Physics*, *116*(A3). Retrieved from https://doi.org/10.1029/2010ja016148
756 Yates, J., Achilleos, N., & Guio, P. (2014). Response of the jovian thermosphere to
757 a transient 'pulse' in solar wind pressure. *Planetary and Space Science*, *91*, 27–
758 44. Retrieved from https://doi.org/10.1016/j.pss.2013.11.009